Dynamics of C$_{60}$ Encapsulation into Single-Wall Carbon Nanotubes

Hendrik Ulbricht and Tobias Hertel*,†

Department of Physical Chemistry, Fritz-Haber-Institut der Max-Planck-Gesellschaft, Faradayweg 4-6, 14195 Berlin, Germany

The encapsulation of C$_{60}$ into single-wall carbon nanotubes (SWNTs) is studied by molecular mechanics and kinetic Monte Carlo trajectory calculations. van der Waals pair-potentials—experimentally derived from the interaction of C$_{60}$ with graphite—are used to calculate three-dimensional C$_{60}$–SWNT potential energy surfaces. We discuss encapsulation via different reaction paths through open tube ends or sidewall defects and compare capture of ballistic C$_{60}$ from the gas phase with encapsulation of C$_{60}$ preadsorbed on the surface of SWNT ropes. Encapsulation of preadsorbed C$_{60}$ is predicted to be the more likely process.

1. Introduction

The synthesis and fabrication of functionalized carbon nanotubes (CNTs) and CNT hybrid structures is a central concern for the use of CNTs in future device technologies. Single-wall carbon nanotubes (SWNTs) have been used as nanoscaled gas sensors,[1] molecular field effect transistors,[2,3] and simple electronic switching devices.[4,5] Future utilization of CNTs will rely increasingly on the successful tailoring of their structural, electronic, and chemical properties.

A novel SWNT hybrid structure with unique electronic properties[6] can be fabricated by the combination of one-dimensional SWNTs with zero-dimensional fullerenes through the encapsulation of C$_{60}$ into SWNTs.[7–9] It has been proposed that encapsulation can be either through the ends of oxidatively opened SWNTs or through defects in their sidewalls. The exact formation mechanism of these "peapods", however, is still under discussion.[10–12]

Here, we study the mechanism of peapod formation using molecular mechanics and dynamics calculations. Three-dimensional potential energy surfaces (PES) for C$_{60}$-SWNT rope interactions are calculated using van der Waals potentials for C$_{60}$–graphene interactions. The latter have been obtained in a previous study, by a measurement of the C$_{60}$–graphite binding energy from thermal desorption measurements.[13] Here, we identify different reaction paths and compare the efficiency of ballistic capture of vapor phase C$_{60}$ with the efficiency expected for encapsulation of C$_{60}$ preadsorbed on the SWNT rope surface. The results suggest that SWNTs may in fact be filled with much higher rates than presently observed.

2. Results and Discussion

2.1. C–C Pair Potentials for the C$_{60}$–SWNT System. The interaction of C$_{60}$ with the graphitic surface of SWNTs is most likely dominated by dispersion forces.[14] This is similar to interactions in solid C$_{60}$ where only 10% of the cohesive energy arises from electrostatic and 90% from van der Waals (vdW) forces.[15] The contribution of electrostatic interactions from polarized bonds of the C$_{60}$ molecule with the graphene surface of SWNTs is expected to be small because C–C bonds in the

curved SWNT graphene sheet do not exhibit a polarization comparable to that observed in C$_{60}$. Polarized bonds at open SWNT ends or in their sidewalls might play a similar role for the C$_{60}$–SWNT interaction as electrostatic forces in solid C$_{60}$. The attractive and repulsive contributions of the latter, however, average out once molecular rotations above a critical temperature set in—as for bulk C$_{60}$ where rotational melting at 260 K leads to the sc- to fcc-phase transition.[15] Here, we do not explicitly consider the influence of different functionalities that might terminate unsaturated carbon bonds at tube openings. One may speculate, however, that electrostatic forces arising from polarized bonds of hydrogen-terminated carbons or oxygen functional groups, for example, do not play an important role at higher temperatures due to small bond polarization in the C$_{60}$ molecules. Covalent interactions on the other hand are supposed to be small due to the fact that all valencies of C$_{60}$ are expected to be saturated. Above room temperature, i.e., at temperatures of relevance for experimental encapsulation runs, we thus assume that electrostatic interactions do not contribute significantly and the dominant interactions arise from dispersion forces. As a consequence, the potential energy V of C$_{60}$ interacting with a tube rope can be approximated by summation of Lenard-Jones pair-potentials V_{LJ}:

$$V = \sum_{i,j} V_{LJ}(r_{ij}) \quad (1)$$

where the index i runs over all atoms in the tube and j includes all atoms in the fullerene. The Lenard-Jones potential is given by

$$V_{LJ}(r_{ij}) = \frac{C_{12}}{r_{ij}^{12}} - \frac{C_6}{r_{ij}^6} \quad (2)$$

where the C_{12} and C_6 coefficients determine the strength and equilibrium distance of the carbon–carbon atom pair-potential. These coefficients should be chosen such that material properties, as binding or cohesive energies, compressibilities or equilibrium lattice parameters can be well reproduced with the resulting potential. For the interaction between individual graphene layers in graphite such considerations lead to (C_6,C_{12}) values of (15.2 eV Å^6, 24100 eV Å^{12}).[16,17] van der Waals interactions between C$_{60}$ molecules in the bulk phase are best described by (18.54 eV Å^6, 28991 eV Å^{12}).[15] Until recently,

* Corresponding author. E-mail: hertel@fhi-berlin.mpg.de.
† Present address: Department of Physics and Astronomy, Vanderbilt University, Nashville, TN 37235.
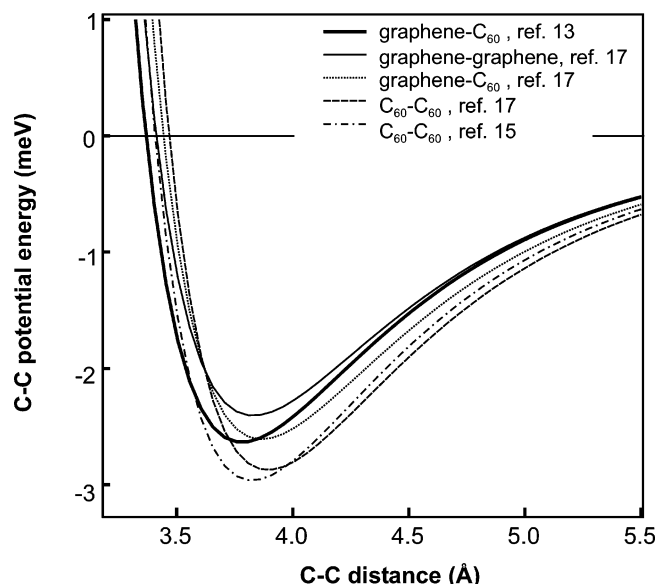
Figure 1. Previously suggested van der Waals pair potentials for interacting carbon atom pairs in different systems. The thick solid line corresponds to the potential used in the present study.

Figure 2. (a) Schematic illustration of tube terminations and local tube-end geometries for a slanted and hexagonally stacked tube array (here a '"rope" of straws). (b) triple (10,10) SWNT arrangement which exhibits all major structural features and possible encapsulation paths found in the larger rope above: (1) encapsulation over the lip of isolated tube ends, (2) and (3) encapsulation paths over the lip of nonisolated tube ends, (4) head-on encapsulation from a groove, and (5) encapsulation through defect openings.

however, no experimental data was available for a determination of C_{60}−graphene and C_{60}−SWNT vdW interactions. Parameters for C_{60}−SWNT interactions were thus frequently derived from graphene−graphene and C_{60}−C_{60} vdW parameters using the Lorentz−Berthelot mixing rules. So far, only a few theoretical predictions of fullerene−graphite or fullerene−SWNT vdW interactions exist, and binding energies calculated for C_{60} encapsulated into SWNTs range from 0.43 to 3.26 eV per ball.[11,12,18,19] To obtain an alternative estimate of the C_{60}−SWNT binding energies from experimental data, we have recently performed a thermal desorption study which allowed us to determine the C_{60}−graphite binding energy of 0.85 eV per molecule from the activation energy for desorption of 1.69 eV. This is slightly larger than previous theoretical predictions.[20] The vdW parameters obtained from our experimental study for the C_{60}−graphite system were $C_6 = 15.4$ eV $Å^6$ and $C_{12} = 22500$ eV $Å^{12}$.[13] For the following calculation of the C_{60}−SWNT rope PES and C_{60}−SWNT binding energies, we will use this set of vdW parameters. The carbon−carbon vdW pair-potentials resulting from these and other previously published vdW parameters are summarized in Figure 1.

2.2. Sample Geometry, Potential Energy Surfaces, and Reaction Paths. Conceivable reaction mechanisms that will be compared in this study are (a) encapsulation through different entry ports via ballistic capture of vapor phase C_{60}, and (b) encapsulation of migrating C_{60} preadsorbed on the surface of a SWNT rope. In addition, for adsorbed C_{60} there are a number of possible reaction paths by which the molecule can enter SWNTs. This is illustrated schematically in Figure 2. In principle, encapsulation can occur either through oxidatively opened SWNT ends or through defects in their sidewalls. Close inspection of the rope-model in Figure 2a reveals that adsorbed C_{60} can enter tubes along one of only 4 distinct reaction paths: (i) encapsulation over the lip of an isolated tube end (labeled (1) in Figure 2b), (ii) encapsulation over the lip of a tube with neighboring SWNTs (labeled (2) or (3)), (iii) "head-on" encapsulation through the open end of a tube (labeled (3)), and (iv) encapsulation through a sidewall opening (labeled (5)). All of these reaction paths can be studied on the small section of a rope shown in Figure 2b.
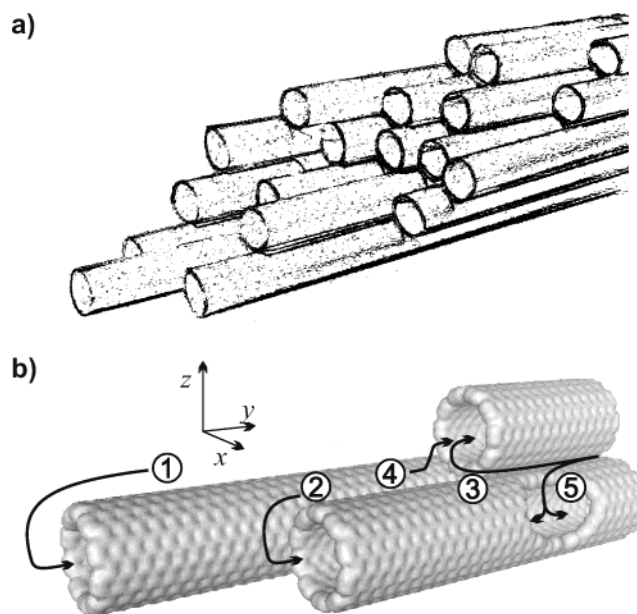
We restricted our study to a rope composed of (10,10) tubes with a diameter of 1.4 nm, as smaller diameters will not permit encapsulation due to steric constraints.[17,21] The triple (10,10) tube configuration in the lower part of Figure 2 exhibits all structural features that are expected to be relevant for the encapsulation dynamics in real systems. It has an individual open end, open ends on top of grooves, and a defect opening in a tube's sidewall. The defect opening here has a length of 18 Å and extends from one side of the tube to the other, i.e., the opening in the tube lattice has a depth of one-half the tube diameter. Irregularities in the termination of sidewall or tube end openings are difficult to predict but are not expected to lead to qualitative changes of the encapsulation efficiency along different reaction paths.

Rotational or vibrational degrees of freedom of C_{60} or the SWNTs are not included in the simulations as their contribution would not lead to significant changes of the location or height of the barriers limiting encapsulation rates as discussed further below.

In the following we begin with a discussion of features characteristic of the three-dimensional C_{60}−SWNT-rope PES calculated from the interaction of an individual C_{60} molecule with the small tube rope in Figure 2b. The topology of this PES will govern the local concentration and distribution of C_{60} on the rope surface. The shape of the PES−in particular in the neighborhood of tube openings−will of course also be of crucial importance for the kinetics of the encapsulation process. A two-dimensional cut through the three-dimensional PES near the opening of the individual tube is shown in the inset of Figure 3. Contour lines are spaced 0.2 eV starting at −0.1 eV. The minimum energy path from the outside of the tube into its interior is marked by the dashed line. The potential energy along this reaction path is also plotted in Figure 3. Here, encapsulation would proceed from left to right starting with a binding energy of 0.54 eV on the external tube surface and ending at 3.01 eV binding energy inside of the tube. A slightly larger binding
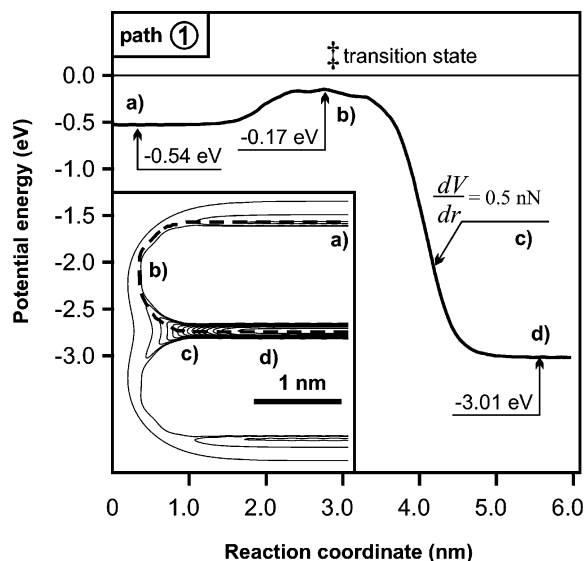
Figure 3. C$_{60}$ encapsulation from the external surface over the lip of an individual (10,10) tube. The inset shows a contour plot of the potential energy surface cutting through the center of this tube near its end. Contours start at −0.1 eV, their spacing is 0.2 eV. The dashed line indicates the minimum energy path. The lip barrier at the end of the tube prevents adsorbed C$_{60}$ from spontaneous encapsulation.

Figure 4. Potential energy surface of C$_{60}$ adsorbed on the external rope surface (line spacing as Figure 3). The pronounced minimum in the center leads to strong lateral confinement of adsorbed C$_{60}$ in the grooves. This is also evident from the scatter plot of statistically chosen (x,z) initial conditions used for the trajectory calculations (see inset). The potential along the dashed line is shown in the lower part of the figure.

energy of 3.26 eV for C60@(10,10) SWNT was previously reported by Girifalco and Hodak using vdW potential parameters derived from graphene and C$_{60}$ interactions by the Lorentz−Berthelot mixing rules.[18] Figure 3 also reveals an important feature of this and other encapsulation paths, namely, the barrier at the lip edge (here 0.34 eV high) which prevents C$_{60}$ from spontaneous encapsulation. This "lip-barrier" (LB) is due to the reduced coordination if C$_{60}$ is located near the lip edge and is thus of character similar to those of the familiar Schwobel-Ehrlich barriers near step edges on solid surfaces.[22,23] In fact, we find that similar LBs are a common feature of all reaction paths.

Evidently, the driving force behind the experimentally observed encapsulation is the strongly exothermic "reaction" as C$_{60}$ moves over the lip into the interior of the tube. The steep descent of the potential at the entrance of the tube provides large forces acting on C$_{60}$ molecules of the order of 0.5 nN comparable to the force exerted on the ball if a pressure of nearly 1 GPa is applied.

The potential energy in the $x-z$ plane which cuts perpendicular through the two lower tubes of Figure 2b is shown in Figure 4. The contour plot reveals the laterally strongly confined adsorption minimum between two neighboring tubes—commonly referred to as the groove site. Due to the 2-fold coordination of C$_{60}$ in these grooves, the potential energy at the minimum is found to be −1.02 eV—i.e., almost exactly twice the binding energy on the external surface of an isolated tube. Under equilibrium conditions, one thus expects to find the majority of adsorbed C$_{60}$ in these grooves, while the remainder of the rope surface should be practically empty. This becomes clearer from the scatter plot of the center of mass positions for a thermal C$_{60}$ distribution at $T = 650$ °C in the inset of Figure 4 (see discussion below for further details). This distribution is rather narrow and gathers the majority of C$_{60}$ molecules within a small region of less than 0.1 nm width.

The head-on reaction path (labeled (4) in Figure 2b) starts in one of these grooves. The corresponding 2D cut through the 3D PES passing through the middle of the target tube is shown in Figure 5, along with the minimum energy reaction path. At
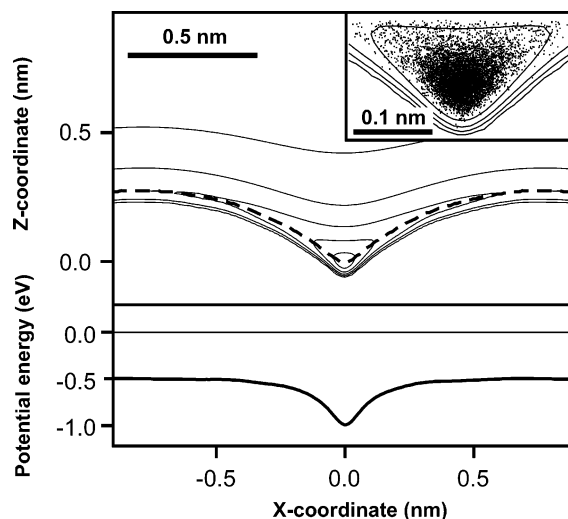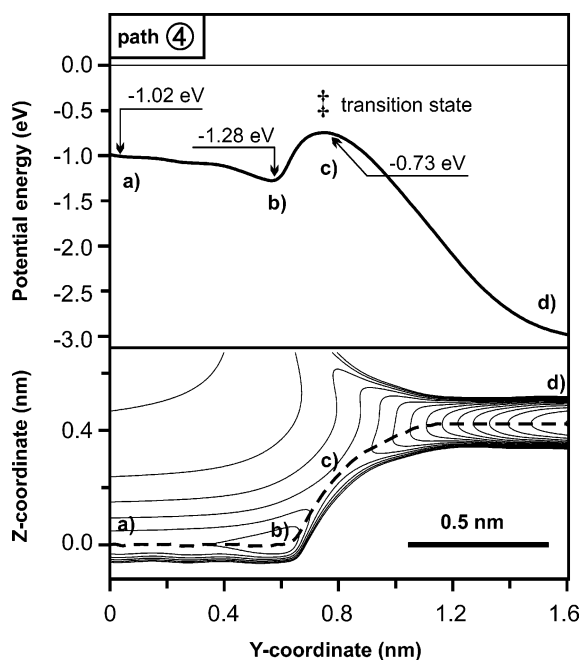

Figure 5. Minimum energy path for encapsulation of adsorbed C$_{60}$ from the groove over the lip of a (10,10) tube (from left to right). The inset shows a contour plot of the potential energy surface cutting through the center of the groove and the target-tube end. The spacing of contour lines starting at −0.1 eV is 0.2 eV. As for the situation illustrated in Figure 3, the barrier at the end of the tube again prevents adsorbed C$_{60}$ from spontaneous encapsulation.

the lip of the tube, we again find a pronounced 0.29 eV high barrier if measured relative to the energy in the groove or 0.55 eV high if measured with respect to the shallow local minimum at the lip of the target tube. The transition state at −0.73 eV—marked by a double cross—is significantly lower in energy than the corresponding transition state of the individual tube at −0.17 eV (see Figure 3). This has important consequences for the encapsulation kinetics as a much higher number of C$_{60}$ molecules will have a thermal energy sufficient to overcome
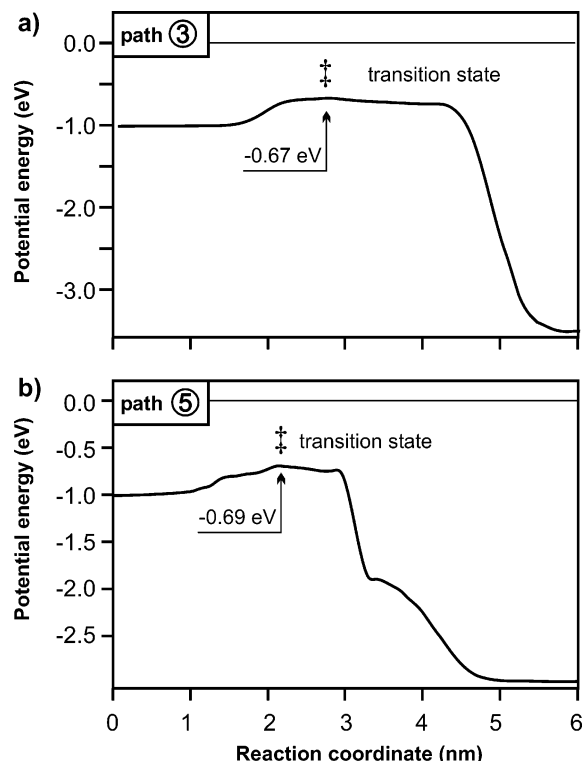
a)

b)

Figure 6. (a) Minimum energy path for encapsulation of adsorbed C_{60} from the groove over the lip of a nonisolated (10,10) tube (from left to right). (b) Minimum energy path for encapsulation through a sidewall defect.

the lower barrier. The C_{60} vibrational potential perpendicular to the reaction path becomes considerably softer at the transition state.

The reaction paths labeled (2) and (3) for capture of C_{60} starting from the groove over the lip of a nonisolated tube are very similar to one another. The minimum energy path for such a process (path (3)) along with the reaction path for encapsulation through a sidewall defect (path (5)) is shown in Figure 6. As for paths (1) and (4), the barriers along paths (2) and (3) are due to the lower coordination of C_{60} at the lip of the tube. The height of barriers with respect to the entrance channel potential well of 0.35 and 0.33 eV for paths (3) and (5), respectively, is very similar to the barrier encountered at the lip of an individual tube which was 0.37 eV high.

2.3. Molecular Dynamics Calculations. Trajectories are propagated by the velocity Verlet algorithm [24] were the center of mass coordinates r_i ($i = x,y,z$) and velocities v_i are computed from the force field F_i using

$$r_i(t + \Delta t) = r_i(t) + \Delta t v_i(t) + \frac{\Delta t^2}{2} \frac{F_i(r(t))}{m} \qquad (3)$$

$$v_i(t + \Delta t) = v_i(t) + \Delta t \frac{F_i(r(t + \Delta t)) + F_i(r(t))}{2m} \qquad (4)$$

The time step Δt should be at most one-tenth of the shortest vibrational period of the system which is approximately 1 ps in the case of encapsulated C_{60}. Here, the increment was typically of the order of 10 fs. The number of trajectories with an energy above the transition state for a particular encapsulation path was typically 10^5.

Initial conditions are chosen such that each relevant degree of freedom contributes $1/2 \ k_B T$ to the total—, i.e. sum of potential- and kinetic- energy, where T is the temperature during
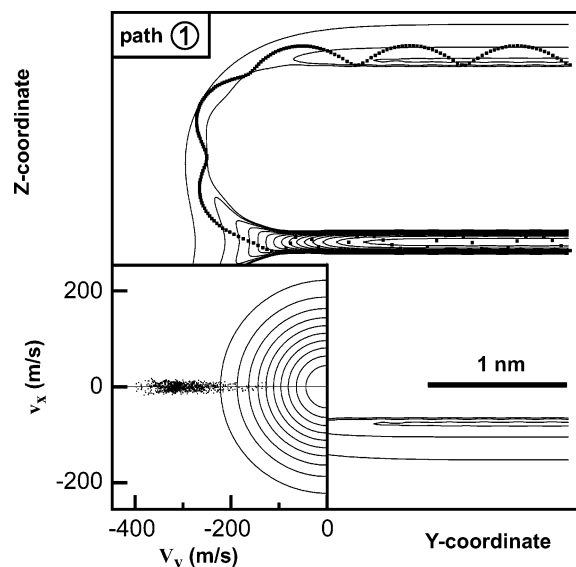

Figure 7. A typical successful trajectory for encapsulation over the lip of an individual tube. Dots indicate trajectory snapshots in 0.1 ps intervals. The inset shows a combined contour and scatter plot of the initial x and z momentum distribution and the initial conditions leading to successful encapsulation, respectively. The strongly forward peaked distribution of successful attempts clearly shows how angular momentum—which is proportional to v_z—can prevent successful encapsulation.

encapsulation runs of typically 650 °C. For a harmonic potential, this would lead to Gaussian space- and momentum-distributions—corresponding to the thermal average of quantum mechanical wave functions of a harmonic oscillator with $\hbar \cdot \omega \ll k_B T$. In the case of a nonharmonic potential as in the groove sites shown in Figure 4, we obtain a nonisotropic real space probability distribution seen in the inset of Figure 4. The velocity distributions in the x, y, and z directions are Gaussian with a variance $\Delta v_{x,y,z}$ of $(k_B T/m)^{1/2}$ identical to that of a free gas.

In Figure 7 we plotted a successful trajectory for encapsulation over the lip of an individual tube (path (1)). The trace corresponds to a projection of the trajectory on the $y-z$ plane with dots marking center of mass positions at time increments of 0.1 ps. The inset in Figure 7 shows a scatter plot of initial velocities along x and y that lead to successful encapsulation along this reaction path. From the small width of this distribution in the x-direction, one clearly sees that trajectories with a small velocity component in the x-direction are more likely to be successful. This clearly illustrates that angular momentum (here, $L_x \propto v_x$ ($x = 0$)) hinders C_{60} encapsulation. It furthermore underlines the importance of three-dimensional trajectory calculations to account for such effects which would not be recognized in a two-dimensional simulation.

Interestingly, encapsulation over the lip of the individual tube end (path (1)) is the only situation where a strong correlation of encapsulation probability and kinetic energy for motion along the reaction coordinate is observed.

A trajectory for successful encapsulation via the head-on approach (path (4)) is shown in Figure 8 (dots marking center of mass positions at time increments of 0.05 ps). The superposition of all successful encapsulation trajectories along path (4) is also shown as grayscale image plot in the lower part of Figure 8. Successful trajectories for the two remaining reaction paths, i.e. from the groove over lip into the open end (path (3)) or through the defect opening (path (5)), are generally more complex.
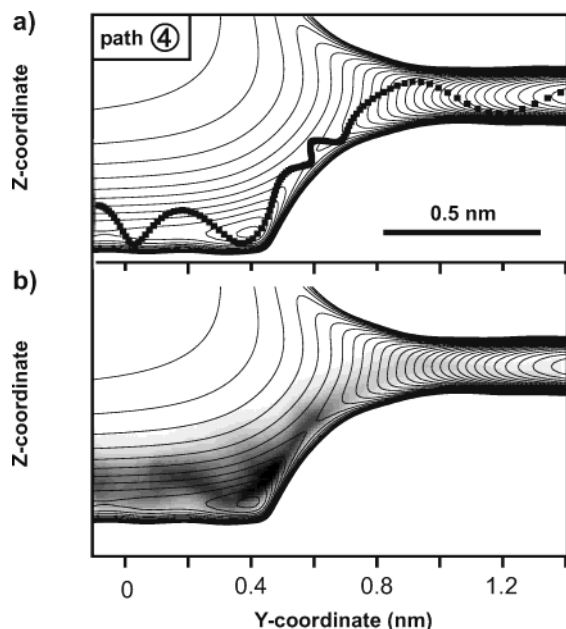
Dynamics of C$_{60}$ Encapsulation into SWNTs

J. Phys. Chem. B, Vol. 107, No. 51, 2003 **14189**

Figure 8. Projection of a successful trajectory for head-on encapsulation on the Y–Z plane at $x = 0$. Dots indicate trajectory snapshots in 0.5 ps intervals. The lower panel shows a combined PES contour and probability density plot averaged over 4×10^4 successful encapsulation trajectories.
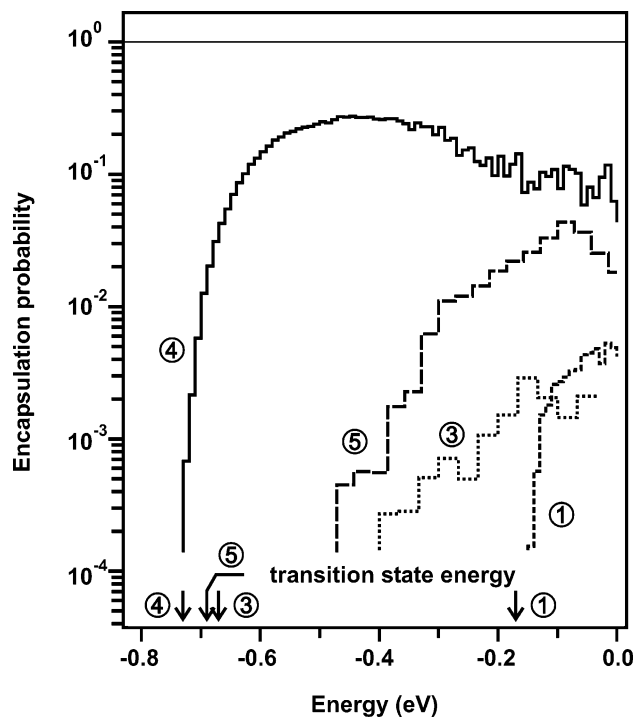

Figure 9. Reaction probabilities via the different paths introduced in Figure 2. Encapsulation via the head-on collision with open tube ends located above a groove (path (4)) is found to have the highest encapsulation probabilities and the lowest threshold.

The results of these calculations are finally summarized in Figure 9 where the encapsulation probabilities $P(E) = N_e(E)/N_i(E)$ are plotted as a function of energy E. $P(E)$ is defined as the ratio of successful N_e and total number of incident trajectories N_i within a certain energy interval. The highest probabilities for encapsulation per attempt are clearly found for the head-on approach via the groove into the open end of the upper tube (path (4)). For this reaction path, the encapsulation probability reaches a maximum of nearly 30%

at an energy of about -0.45 eV, i.e., about 0.25 eV above the transition state energy before it levels off to 10% as the energy approaches the desorption continuum. None of the other reaction paths exhibits comparably high probabilities. Encapsulation via the defect opening is the second likely candidate in this series. The transition-state energy, however, is significantly higher than for the head-on encounter and the maximum of the encapsulation probability is nearly an order of magnitude smaller than for path (4).

2.4. Encapsulation Rates. The change of the endohedral concentration [C$_{60}^{\text{endo}}$] in time, is here obtained from the above molecular dynamics calculations using

$$\frac{d[C_{60}^{\text{endo}}]}{dt} = \bar{P}f_i[O^{\text{SWNT}}] \tag{5}$$

where $\bar{P}$ is the velocity-weighted encapsulation probability of the thermal C$_{60}$ distribution, f_i is the flux of incident C$_{60}$ molecules along the reaction path, and [O$^{\text{SWNT}}$] is the concentration of tube openings per unit length. The incident flux f_i is given by $f_i = [C_{60}^{\text{exo}}]\bar{v}_i$, where $\bar{v}_i$ denotes the mean velocity of molecules incident along the reaction path. [C$_{60}^{\text{exo}}$] denotes the concentration of exohedral C$_{60}$ in the entrance channel of the reaction path. It follows that if we rearrange eq 5 to a rate equation that is first order in [C$_{60}^{\text{exo}}$] and [O$^{\text{SWNT}}$], we obtain

$$\frac{d[C_{60}^{\text{endo}}]}{dt} = k[E^{\text{SWNT}}][C_{60}^{\text{exo}}] \tag{6}$$

where the rate constant k, in units of m/s, is given by

$$k = \bar{P}\bar{v}_i \tag{7}$$

Values for k, $\bar{P}$, as well as $\bar{v}_e$ (the mean velocity of successful trajectories along the reaction path) are summarized in Table 1. At the sample temperature of 650 °C, the mean velocity $\bar{v}_i = (2k_BT/\pi m)^{1/2}$ of incident trajectories propagating along the reaction path is 83 m/s.

The concentration [C$_{60}^{\text{exo}}$] of exohedral C$_{60}$ is estimated from the surface coverage Θ using Langmuir kinetics:

$$\Theta = \frac{bp}{1 + bp} \tag{8}$$

with

$$b = \frac{\sigma}{\nu\sqrt{2\pi m k_B T}} \exp\left(\frac{E_B}{k_B T}\right) \tag{9}$$

where p is the pressure, σ is the area of the adlayer unit cell, and m is the adsorbate mass. The preexponential factor ν of 1.6×10^{13} s^{-1} is obtained from the temperature dependence of the vapor pressure.[13]

For obtaining the C$_{60}$ concentration on the external surface of an individual tube we thus used the corresponding binding energy of -0.54 eV and the surface area covered by a single C$_{60}$ molecule within a close packed 2-dimensional layer of 8.7 $\times 10^{-19}$ m^2. At a temperature of 650 °C and a C$_{60}$ partial pressure of $\sim$10 Pa, this yields a surface coverage of 1.5×10^{-6}. The latter is used to obtain the C$_{60}$ concentration per unit length. To this end we use the circumference of the (10,10) tube and account for the van der Waals distance of the C$_{60}$ molecule and tube. The resulting effective radius of the cylinder surface on which the C$_{60}$ center of mass rests is 1.3 nm. The resulting C$_{60}$ concentration of 1.4×10^4 m^{-1} is about 2 orders

TABLE 1: Summary of Parameters Used for the Calculation of Encapsulation Rates and Rate Constants

reaction path, start of trajectory	E_0 (eV)	$E^{\ddagger}$ (eV)	$\bar{P}$	$\bar{v}_e$ (m/s)	coverage (ML)	$[C_{60}^{exo}]$ (m^{-1})	k (m/s)	f_e (s^{-1})
head-on collision (4) groove	−1.02	−0.73	10%	110	1.2×10^{-3}	1.2×10^6	8	1.0×10^7
defect opening (5) groove	−1.02	−0.69	1.0%	180	1.2×10^{-3}	1.2×10^6	0.8	1.0×10^6
back over lip (2),(3) groove	−1.02	−0.67	0.06%	230	1.2×10^{-3}	1.2×10^6	0.05	6×10^4
end of single tube (1) tube surface	−0.54	−0.17	0.6%	300	1.5×10^{-6}	1.4×10^4	0.5	7×10^3

of magnitude smaller than the equilibrium concentration of 1.1×10^6 m^{-1} expected for adsorption in the exohedral groove sites, mostly due to the nearly 2-fold increase of the binding energy. In the latter case we used a unit cell size of 1.7×10^{-18} m^2 as given by the nearest neighbor C_{60} and (10,10) tube spacing of 1.02 and 1.7 nm, respectively.

The flux f_e of C_{60} encapsulated through a single entry port opening is now calculated from the product of the above concentrations and the corresponding rate constants (see Table 1). In a previous estimate we used slightly different unit cell sizes and obtained the rate of encapsulation from a simple integration of the reaction probabilities in Figure 9 weighted by a Maxwell-Boltzman distribution.[13] The latter neglects any correlation of the encapsulation probability with the kinetic energy along the reaction coordinate and thus leads to quantitatively but not qualitatively different results. The thorough analysis presented here exhibits the same preference of encapsulation by the head-on collision mechanism with the open tube end above the groove. Encapsulation through the defect openings is estimated to be about an order of magnitude less likely and the remaining two reaction paths turn out to be yet another one and 2 orders of magnitude less efficient.

Encapsulation by direct capture of ballistic C_{60} molecules striking the ∼2 Å^2 entry port of an open tube end or defect would be comparatively slow with a success rate of about 10^3 s^{-1}, i.e., yet about another order of magnitude less than encapsulation along the least efficient reaction path for pre-adsorbed C_{60}.

3. Summary

We have studied the kinetics and mechanism of C_{60} encapsulation by SWNTs using molecular mechanics and dynamics simulations. Potential energy surfaces were calculated for a small SWNT rope. Ehrlich-Schwoebel-like lip barriers (LBs) of approximately 0.3 eV height were found to exist near all types of tube openings. Encapsulation of adsorbed C_{60} is thus expected to be an activated process. Nevertheless, we found that encapsulation of C_{60} adsorbed on the SWNTs rope is more efficient than capture of ballistic C_{60} molecules from the vapor. This is mostly due to the high concentration and consequently the high reactant flux of C_{60} adsorbed in grooves on the rope surface under vapor-surface equilibrium conditions. Encapsulation should be most probable for C_{60} adsorbed in grooves by head-on collisions with open tube ends. The high predicted rate

of successful encapsulation attempts suggests that the experimentally observed filling speeds are not limited by the probability that C_{60} molecules find their way to the entrance of an open tube but rather by the rate at which encapsulated C_{60} molecules or chains of molecules migrate inside the tubes. Further experimental work on the kinetics of encapsulation are clearly desirably to understand the encapsulation mechanism in further detail.

References and Notes

(1) Kong, J.; Franklin, N. R.; Zhou, C. W.; Chapline, M. G.; Peng, S.; Cho, K. J.; Dai, H. J. *Science* **2000**, *287*, 622.

(2) Tans, S. J.; Verschueren, A. R. M.; Dekker, C. *Nature* **1998**, *393*, 49.

(3) Martel, R.; Schmidt, T.; Shea, H. R.; Hertel, T.; Avouris, Ph. *Appl. Phys. Lett.* **1998**, *73*, 247.

(4) Derycke, V.; Martel, R.; Appenzeller, J.; Avouris, Ph. *Nano Lett.* **2001**, *1*, 453.

(5) Bachtold, A.; Hadley, P.; Nakanishi, T.; Dekker, C. *Science* **2001**, *294*, 1317.

(6) Hornbaker, D. J.; Kahng, S.-J.; Misra, S.; Smith, B. W.; Johnson, A. T.; Mele, E. J.; Luzzi, D. E.; Yazdani, A. *Science* **2002**, *295*, 828.

(7) Smith, B. W.; Monthioux, M.; Luzzi, D. E. *Nature* **1998**, *396*, 323.

(8) Kataura, H.; Maniwa, Y.; Kodama, T.; Kikuchi, K.; Hirahara, K.; Suenaga, K.; Iijima, S.; Suzuki, S.; Achiba, Y.; Krätschmer, W. *Synth. Metals* **2001**, *121*, 1195.

(9) Smith, B. W.; Russo, R. M.; Chikkannanavar, S. B.; Luzzi, D. E. *J. Appl. Phys.* **2002**, *91*, 9333.

(10) Smith, B. W.; Luzzi, D. E. *Chem. Phys. Lett.* **2000**, *321*, 169.

(11) Qian, D.; Liu, W. K.; Ruoff, R. S. *J. Phys. Chem. B* **2001**, *105*, 10753.

(12) Berber, S.; Kwon, J. K.; Tománek, D. *Phys. Rev. Lett.* **2002**, *88*, 185502.

(13) Ulbricht, H.; Moos, G.; Hertel, T. *Phys. Rev. Lett.* **2003**, *90*, 95501.

(14) Saito, S.; Oshiyama, A. *Phys. Rev. Lett.* **1991**, *66*, 2637.

(15) Lu, J. P.; Li, X.-P.; Martin, R. M. *Phys. Rev. Lett.* **1992**, *68*, 1551; Li, X.-P.; Lu, J. P.; Martin, R. M. *Phys. Rev. B* **1992**, *46*, 4301.

(16) Girifalco, L. A.; Lad, R. A. *J. Chem. Phys.* **1956**, *25*, 693.

(17) Girifalco, L. A.; Hodak, M.; Lee, R. S. *Phys. Rev. B* **2000**, *62*, 13104.

(18) Girard, Ch.; Lambin, Ph.; Dereux, A.; Lucas, A. A. *Phys. Rev. B* **1994**, *49*, 11425.

(19) Girifalco, L. A.; Hodak, M. *Phys. Rev. B* **2002**, *65*, 125404.

(20) Ruoff, R. S.; Hickman, A. P. *J. Phys. Chem.* **1993**, *97*, 2494.

(21) Okada, S.; Saito, S.; Oshiyama, A. *Phys. Rev. Lett.* **2001**, *86*, 3835.

(22) Ehrlich, G.; Hudda, F. G. *J. Chem. Phys.* **1966**, *44*, 1039.

(23) Schwoebel, R. L.; Shipsey, E. J. *J. Appl. Phys.* **1966**, *37*, 3682.

(24) Heermann, D. In *Computer simulation methods in theoretical physics,* 2nd ed.; Springer: Berlin, 1990.